International Journal of Thermal Sciences 51 (2012) 132–144

Contents lists available at SciVerse ScienceDirect

International Journal of Thermal Sciences

journal homepage: www.elsevier.com/locate/ijts

Pore-scale flow and mass transport in gas diffusion layer of proton exchange membrane fuel cell with interdigitated flow fields

Li Chen*, Hui-Bao Luan, Ya-Ling He, Wen-Quan Tao

Key Laboratory of Thermal Fluid Science and Engineering of MOE, School of Energy and Power Engineering, Xi'an Jiaotong University, Xi'an, Shaanxi 710049, China

ARTICLE INFO

Article history:
Received 29 November 2010
Received in revised form
18 May 2011
Accepted 4 August 2011
Available online 14 September 2011

Keywords:
Proton exchange membrane fuel cell
Interdigitated flow field
Lattice Boltzmann method
Pore-scale
Mass transport
Liquid water

ABSTRACT

Lattice Boltzmann method (LBM) is employed to investigate pore-scale flow and mass transport in a carbon paper gas diffusion layer (GDL) of interdigitated PEMFC. The carbon paper GDL is reconstructed using the stochastic method, and its macroscopic transport properties are numerically predicted. The predicted anisotropic permeabilities and effective diffusivity of the reconstructed GDL agree well with existing measurements. Then, effects of the porous structures of the carbon paper GDL are explored in terms of fluid flow, species transport and electrochemical reaction. The GDL porous structures greatly affect flow and mass transport, creating distinct specie concentration distribution and local current density distribution. Besides, simulations are performed to explore liquid water behaviors in the reconstructed GDL. The simulation results present a detailed description of the pore-scale liquid water behaviors. Further, simulations are performed to investigate the effects of land width and GDL contact angle on liquid water removal time and residual saturation. Narrower land reduces liquid water removal time and residual saturation. Higher contact angle increases the removal time and reduces the residual saturation.

1. Introduction

Proton exchange membrane fuel cell (PEMFC) has been considered as an alternative power source for various applications and has caught much attention during the past decades [1], due to its advantages including high power density, low operation temperature, high efficiency, low emissions and low noise. To improve the performance of PEMFC, it is very important to effectively and homogeneously transport the reactant gas into the catalyst layer (CL) for reaction. Usually, this can be obtained by appropriately designing the flow field [2]. One of the famous and efficient flow field design is the interdigitated flow field shown in Fig. 1, proposed by Nguyen [3]. This kind of flow field creates an in-plane pressure gradient in the gas diffusion layer (GDL), hence induces gas flow in the in-plane direction under the land. The in-plane gas flow positively enhances the mass transport by transferring the mass transport mechanism from diffusion to forced convection within the GDL, hence increases the reactant supply to the reactive site [4]. Besides, the in-plane gas flow also removes most of the liquid water accumulated in the GDL, thus significantly alleviating flooding problem in the cathode. Consequently, the interdigitated flow field greatly improves the performance of PEMFC compared to the conventional parallel flow field [5–8].

The performance of PEMFC with interdigitated flow field (hereinafter referred to as intergiditated PEMFC) has been evaluated under different operating conditions and physical parameters. The operating conditions such as air flow rate and humidification of reactants significantly affect the performance of intergiditated PEMFC [4,6,7,9]. Physical parameters including GDL thickness, land width and channel/land width ratio also play important roles on the performance of intergiditated PEMFC. The GDL thickness needs to be optimized to get optimal performance, because thinner GDL may reduce gas flow rate while thicker GDL may increase the diffusion layer thickness [10,11]. Shorter land and higher channel/land width ratio are desirable for better performance as they can increase flow rate in the GDL [10–12]. Besides, the performance of interdigitated PEMFC is also greatly affected by liquid water content in the GDL. Accordingly, He et al. [13] and Ito et al. [14] estimated the liquid water content in the GDL by measuring pressure drop between the inlet and outlet GC.

The microscopic structures and characteristics of GDL also significantly influence the performance of interdigitated PEMFC. Generally, the GDL is fabricated by carbon fiber based carbon paper or carbon cloth. The GDL shows complex structures with heterogeneous characteristics. Concretely, these heterogeneous characteristics present as heterogeneous porosity, wettability, effective

* Corresponding author. Tel.: 86 029 82669106.
E-mail address: dandaoxingtianya@163.com (L. Chen).

1290-0729/$ – see front matter
doi:10.1016/j.ijthermalsci.2011.08.003

diffusivity and permeability in the GDL. The pore sizes of the GDL randomly distribute, ranging from a few microns to tens of microns. The surface wettability within the GDL is usually non-uniform, because hydrophilic and hydrophobic pores generally coexist within the GDL, due to possible non-uniform loading of PTFE [15]. In addition, the permeability and effective diffusivity also show heterogeneous characteristics due to the selective orientations of carbon fibers [16–19]. These heterogeneous characteristics, specially the anisotropic permeability, are more concerned in the GDL of interdigitated PEMFC due to the air flow induced in the in-plane direction [20]. However, previous work based on macroscopic continuum models [5–7,10–12], while with the advantage of numerical efficiency, suffers the disadvantage of neglecting the influence of actual structures and related heterogeneous characteristics of GDL. Due to this neglect, macroscopic continuum models have to employ many flow empirical relations. The accuracy of some of these empirical relations applied to GDL materials is questionable, as they sometimes predicted unreasonable distributions in GDL [21]. Therefore, these empirical relations still need further validation.

More fundamental models and simulations considering the actual structures of GDL are currently required to fully understand fluid flow and mass transport. Pore-network model and lattice Boltzmann method (LBM) are useful numerical tools for this purpose. The pore-network model partly considers the microscopical porous morphology of GDL by modeling the GDL as a regular cubic network of pores connected by throats. Recently, several studies adopting this model have been reported to investigate the distribution of liquid water in GDL [16,21,22] and to obtain the GDL specific capillary pressure versus saturation correlation [23]. Compared to pore-network model which approximately describes porous morphology of GDL, LBM can simulate fluid flow and mass transport based on real structures of GDL [24]. There have been several studies adopting LBM to investigate the transport processes and structural properties in GDL [22,25–30]. In a two dimensional (2D) GDL with actual porous structures, Park et al. [27] simulated the liquid water behaviors and presented a vivid account of the pore-scale behaviors of a liquid droplet. Further, simulation is performed in 3D carbon paper GDL reconstructed by the stochastic method [22,25,28,29]. Mukherjee et al. [28] investigated the effects of porous structures on liquid water transport process. Hao and Cheng [29] explored the effect of GDL wettability on liquid water transport and distribution. Besides, the anisotropic permeability of the GDL is also numerically predicted [25,30]. These researches indeed presented a detailed insight into the pore-scale information of flow and mass transport within the GDL, although simulations using LBM always require huge computational resources.

In this paper, we go on further to investigate the pore-scale flow and mass transport processes in the GDL of interdigitated PEMFC by employing LBM, based on aforementioned work. We focus on the effects of local porous structures of GDL on fluid flow, species transport, local current density distribution, and liquid water dynamic behaviors. Besides, we investigate the effects of land width and GDL contact angle on liquid water removal time and residual saturation. The remaining part of this paper is organized as follows: LBM models used in this study are briefly introduced in Section 2. In Section 3, the computational domain is presented which includes a carbon paper GDL obtained from reconstruction process. In Section 4, the anisotropic permeability and effective diffusivity of the porous GDL reconstructed are numerically predicted and compared with existing measurements. Then, effects of GDL porous structures on fluid flow, mass transport, local current density distribution, and pore-scale liquid water behaviors are investigated. Finally, a conclusion is obtained in Section 5.

2. Brief introduction to LBM

During the last two decades, LBM has been developed as an alternative and powerful numerical scheme for a variety of fluid transport phenomena [24]. Unlike conventional CFD methods which solve discrete forms of the mass, momentum and energy conservation equations based on macroscopic quantities such as velocity and density, LBM simulates fluid particles on a mesoscopic level based on Boltzmann equation using a small number of velocities adapted to a regular grid in space. For completeness, only a brief introduction of LB models is given in the following paragraphs.

2.1. Fluid flow LB model

The flow LB model employed in this study is based on the simple and popular Bhatnagar-Gross-Krook (BGK) method [31]. DnQb lattice is adopted where n denotes the dimension and b represents the number of discrete velocities. The evolution equation for particle distribution function $f_i(x,t)$ is

$$f_i(x+\mathbf{e}_i\Delta t, t+\Delta t) - f_i(x,t) = -\frac{1}{\tau}\left(f_i(x,t) - f_i^{\mathrm{eq}}(x,t)\right) \tag{1}$$

where Δt is the time increment and τ is the collision time related to the kinematical viscosity. $\mathbf{e}_i$ is the discrete velocities and is defined as (for D2Q9 model used in this study).

$$\mathbf{e}_i = \begin{cases} 0 & i=0 \\ \left(\cos\left[\frac{(i-1)\pi}{2}\right], \sin\left[\frac{(i-1)\pi}{2}\right]\right) & i=1,2,3,4 \\ \sqrt{2}\left(\cos\left[\frac{(i-5)\pi}{2}+\frac{\pi}{4}\right], \sin\left[\frac{(i-5)\pi}{2}+\frac{\pi}{4}\right]\right) & i=5,6,7,8 \end{cases} \tag{2}$$

The equilibrium distribution function $f_i^{\mathrm{eq}}(x,t)$ is given as

$$f_i^{\mathrm{eq}} = w_i\rho\left[1 + \frac{\mathbf{e}_i\cdot\mathbf{u}}{(c_s)^2} + \frac{(\mathbf{e}_i\cdot\mathbf{u})^2}{2(c_s)^4} - \frac{\mathbf{u}\cdot\mathbf{u}}{2(c_s)^2}\right] \tag{3}$$

for D2Q9 model, weight factor w_i are $w_i = 4/9$, $i = 0$; $w_i = 1/9$, $i = 1,2,3,4$; $w_i = 1/36$, $i = 5,6,7,8$. c_s is the sound speed ($c_s = c/\sqrt{3}$ where c equals $\Delta x/\Delta t$). The fluid number density ρ and velocity $\mathbf{u}$ are obtained from the first and second moments of the particle distribution functions.

$$\rho = \sum_i f_i, \tag{4}$$

$$\rho\mathbf{u} = \sum_i f_i\mathbf{e}_i \tag{5}$$

The kinematics viscosity in lattice unit is related to the collision time by

$$\upsilon = c_s^2(\tau_\upsilon - 0.5)\Delta t \tag{6}$$

2.2. Mass transport LB model

For mass transport with reaction, the evolution equation of the distribution function is [32]

$$f_i(x+\mathbf{e}_i\Delta t, t+\Delta t) - f_i(x,t) = -\frac{1}{\tau}\left(f_i(x,t) - f_i^{\mathrm{eq}}(x,t)\right) + S \tag{7}$$

where S is the source term related to the reaction and will be discussed in Section 4.3. The equilibrium distribution function $f_i^{\mathrm{eq}}(x,t)$ is commonly chosen as [33]

$$f_{i,k}^{eq} = X_k[J_i + K_i \mathbf{e}_i \cdot \mathbf{u}]. \quad (8)$$

where K_i is constant and equals 1/2 for two dimension simulation. Subscript k denotes the kth component and X_k is the mole fraction of kth component (the ratio between the concentration of k component and the total concentration). J is the rest fraction and is obtained from $\sum f_i = \sum f_i^{eq}$.

For mass transport simulation, the D2Q9 square lattice for 2D simulation can be reduced to D2Q5 square lattice without loss of accuracy [33]. Therefore, the discrete velocities are

$$\mathbf{e}_i = \begin{cases} 0 & i = 0 \\ \left(\cos\left[\frac{(i-1)\pi}{2}\right], \sin\left[\frac{(i-1)\pi}{2}\right]\right) & i = 1,2,3,4 \end{cases} \quad (9)$$

and J_i in Eq. (8) is given by [33]

$$J_i = \begin{cases} J_0, & i = 0 \\ (1 - J_0)/4, & i = 1,2,3,4 \end{cases} \quad (10)$$

where the rest fraction J_0 can be selected from 0 to 1. Species mole fraction X_k is obtained by

$$X_k = \sum_i f_{i,k} \quad (11)$$

The diffusivity in lattice unit is related to the collision time by

$$D = C_Q(1 - J_0)(\tau_D - 0.5)\frac{\Delta x^2}{\Delta t} \quad (12)$$

where C_Q is a lattice dependent coefficient and equals 1/2 for 2D simulation [33].

2.3. Multiphase LB model

In this study, multi-component multiphase model with inter-particle forces proposed by Shan and Chen (SC model) [34,35] is employed to investigate the two-phase flow in GDL. The inter-particle forces are included in the kinetics through a set of potentials. In SC model it is simple to involve these interactions by replacing $\mathbf{u}$ in Eq. (3) with

$$\mathbf{u}_k = \mathbf{u}' + \frac{\tau_k \mathbf{F}_k}{\rho_k} \quad (13)$$

where k denotes the kth fluid component. $\mathbf{u}'$ is a common velocity for all of the phases (liquid water and air in this paper) defined as

$$\mathbf{u}' = \frac{\sum_k \rho_k \mathbf{u}_k/\tau_k}{\sum_k \rho_k/\tau_k} \quad (14)$$

In Eq. (13), $\mathbf{F}_k$ is the total force acting on the kth phase which may include fluid–fluid surface tension force, fluid–solid adhesion and body forces. The total fluid–fluid surface tension force acting on the particles of the kth component at lattice site x is defined as [36]

$$\mathbf{F}_{c,k} = -\psi_k(\rho_k(x)) \sum_{x'} \sum_{\bar{k}}^{s} G_{k\bar{k}}(x,x')\psi_{\bar{k}}(\rho_{\bar{k}}(x'))(x' - x) \quad (15)$$

The effective density $\psi_k(\rho_k)$ is defined as $\psi_k(\rho_k) = \rho_0(1 - \exp(-\rho_k/\rho_0))$. If only the surface tension forces between the nearest and next-nearest neighboring points are considered, G can be described as

$$G_{k\bar{k}}(x,x') = \begin{cases} 4g & |x - x'| = 1 \\ g & |x - x'| = \sqrt{2} \\ 0 & |x - x'| = 0 \end{cases} \quad (16)$$

where g controls the strength between fluids. The fluid–solid interaction force $\mathbf{F}_{a,k}$ is introduced to describe the interaction between kth fluid and solid walls [36]

$$\mathbf{F}_{a,k} = -\psi_k(\rho_k(x)) \sum_{x'} W(x,x')s(x')(x' - x) \quad (17)$$

$$W(x,x') = \begin{cases} 4w & |x - x'| = 1 \\ w & |x - x'| = \sqrt{2} \\ 0 & |x - x'| = 0 \end{cases} \quad (18)$$

where s is an indicator function and equals 0 and 1 for pore and solid, respectively. The coefficient w, which controls the strength between fluid and wall, is positive for non-wetting fluid and negative for wetting fluid. Different wettability can be obtained by adjusting w.

After involving inter-particle forces in Eq. (13), the relationship between pressure and density becomes [35]

$$p = \rho c_s^2 + \frac{3}{2}\sum g_{k\bar{k}}\ \psi_k\psi_{\bar{k}} \quad (19)$$

This can be considered as the equation of state (EOS) of a non-ideal fluid, which makes the separation of liquid phase and gas phase possible.

3. Computational domain

The blue dashed rectangle in Fig. 1(b) schematically shows the computational domain in this study, which consists of a half of inlet channel, a half of outlet channel, a land, a GDL and a CL. The CL is

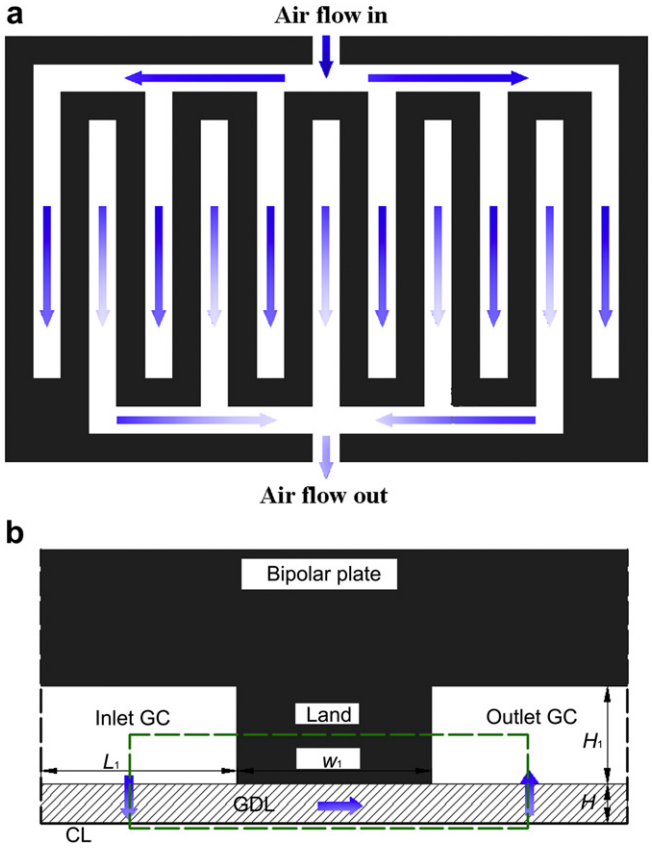

Fig. 1. Schematic of the cathode of PEMFC with interdigitated flow field: (a) top view, (b) side view.

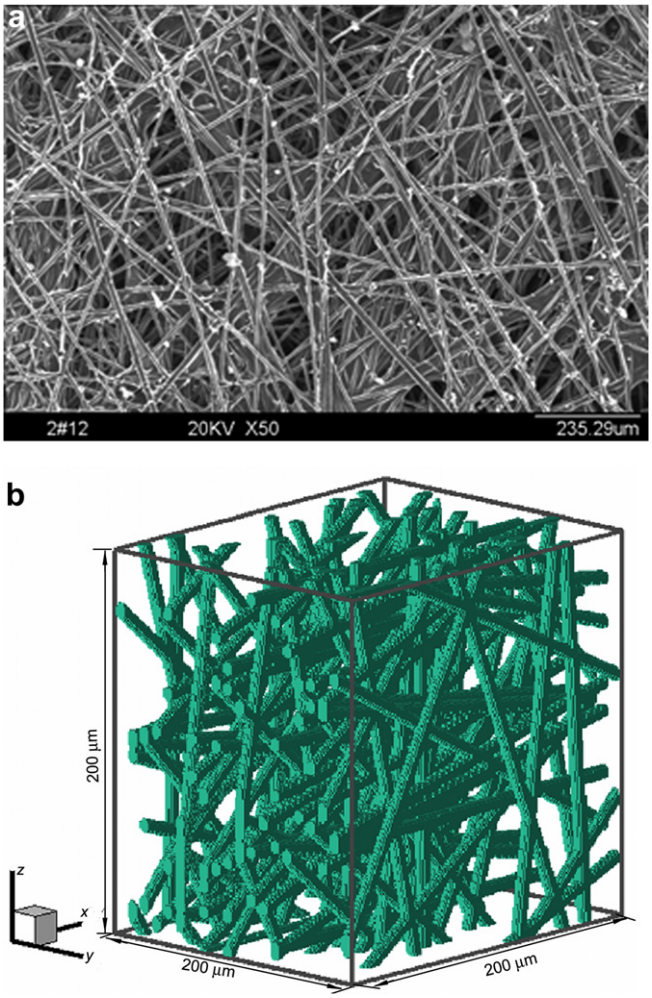

Fig. 2. Microstructures of the carbon paper GDL. (a) SEM image of a carbon paper GDL, (b) 3D structure of the reconstructed GDL.

simply treated as an ultra-thin interface on the bottom surface of the GDL. A GDL with complex porous structure obtained from 3D structure reconstruction process is used instead of a homogenous GDL.

The 3D reconstruction of GDL is based on the statistical information of carbon paper GDL. Fig. 2(a) shows a SEM image of a carbon paper GDL. The carbon paper GDL consists of randomly distributed carbon fibers in the in-plane direction, leading to different in-plane and through-plane properties. Following assumptions are made in the 3D reconstructed process for simplification based on the observation of Fig. 2(a): the carbon fibers are straight with fixed diameter, no fiber is orientated for the through-plane direction and intersecting carbon fibers are randomly distributed in the in-plane direction. Then, the reconstruction procedure is implemented by piling up several carbon fiber layers. Each of the carbon fiber layers can be generated by locating fibers with random positions and angles until the prescribed porosity in this layer is satisfied. Fig. 2(b) shows a 3D GDL generated from the reconstruction with fiber diameter of 7 μm, porosity of 0.7 and total layer number of 24, where x or z is the through-plane direction and y is the in-plane direction.

A cross-section of the 3D reconstructed GDL is selected and serves as the 2D porous GDL in the computational domain, as shown in Fig. 3. The porosity of the cross-section is 0.87. Table 1 lists dimensions of the computational domain in Fig. 3. The computational domain is meshed by 2000 × 240 grids which are proved to be proper after grid-dependency tests with three sets of meshes of 1500 × 180, 2000 × 240 and 2400 × 288.

Table 1
Physical parameters.

Quantity	Value
Dimensions of the computational domain	
Width of the inlet/outlet channel, L_1	1000 μm
Width of the land, W	1000 μm
Height of the GDL, H	200 μm
Operating conditions	
Pressure of the operation condition, P	5.0 × 101 325 Pa
Temperature of the operation condition, T	353 K
Universal gas constant, R	8.314 J mol^{-1} K^{-1}
Faraday's constant, F	96 487 C mol^{-1}
Air inlet velocity, u	1.5 m s^{-1}
Inlet mole fraction rate of oxygen, $X_{O,in}$	0.21
Inlet mole fraction rate of nitrogen, $X_{N,in}$	0.79
Inlet mole fraction rate of water vapor, $X_{w,in}$	0.0
Open circuit potential, V_{oc}	1.1 V [5]
Reference oxygen concentration, $C_{O,ref}$	1.2 mol m^{-3} [41]
Diffusivity of oxygen in air, D_O	2.84 × 10^{-5} m^2 s^{-1} [16]
Diffusivity of water vapor in air, D_H	3.55 × 10^{-5} m^2 s^{-1} [16]
Cathode transfer coefficient, α	1.0 [8]
ORR reduction order, γ_c	1 [9]
Cathode exchange current density multiply specific area, $A_v\, j_{ref}$	110 A m^{-3} [8]

4. Results and discussion

In the LBM model, the simulation variables are in the lattice units instead of physical units. To connect the lattice space to physical space, length scale l_0, time scale t_0 and density scale ρ_0 are chosen in this study. Accordingly, the physical variables such as velocity u_p, pressure p_p, permeability k_p, viscosity υ_p and diffusivity D_p can be calculated from the quantities in lattice system (subscripted by L) as follows

$$u_P = u_L\frac{l_0}{t_0}, p_P = p_L\rho_0\left(\frac{l_0}{t_0}\right)^2, k_P = k_L l_0^2, D_P = D_L\frac{l_0^2}{t_0}, \upsilon_P = \upsilon_L\frac{l_0^2}{t_0} \quad (20)$$

In this study, the scale parameters are chosen as $l_0 = 1.0 \times 10^{-6}$ m, $t_0 = 1.33 \times 10^{-8}$ s and $\rho_0 = 1.0$ kg m^{-3}.

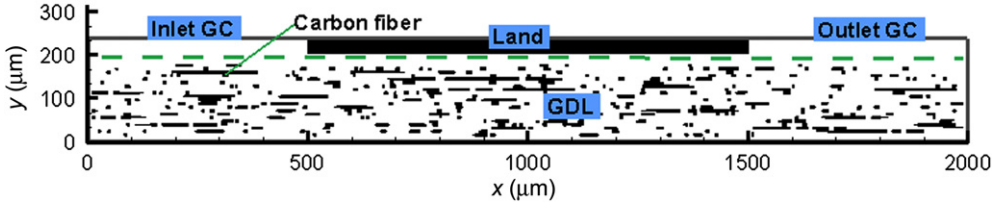

Fig. 3. Computational domain including the reconstructed porous GDL.

In the following sections, the permeability and effective diffusivity of the porous carbon paper GDL are numerically evaluated and compared with the experimental results. Then single-phase simulations using the flow LB model and mass transport LB model are performed to predict gas flow, concentration distribution and local current density distribution in the GDL in Section 4.3. Finally, two-phase LB model is applied to simulate pore-scale behaviors of liquid water in the GDL in Section 4.4.

4.1. Permeability of the porous GDL

The permeability is one of the most important macroscopic effective transport properties of the porous GDL, which is inhomogeneous due to the fiber orientation. Usually, the in-plane permeability is higher than the through-plane permeability [18]. To evaluate the permeability of the 2D porous GDL generated in Section 3, air flow simulation is performed for the in-plane direction (x direction) and through-plane direction (y direction) using flow LB model introduced in Section 2.1, respectively. For in-plane flow, pressure boundaries are specified at the inlet and outlet, respectively (left and right boundaries of GDL in Fig. 3), and solid boundaries are specified on the rest surfaces (top and bottom boundaries of GDL in Fig. 3). For the through-plane flow, pressure boundaries are specified on the inlet and outlet, respectively (top and bottom boundaries of GDL in Fig. 3), keeping the rest surfaces as solid boundaries (left and right boundaries of GDL in Fig. 3). The solid obstacles in the domain are impermeable objects with no slip boundary condition on their surfaces. To reduce the influence of the solid obstacles on the inlet and outlet boundaries, fifty more lattices are added on the inlet/outlet boundary as buffer zones. The permeability of the porous GDL can be calculated according to the Darcy' law

$$K = -\frac{\mu\langle u\rangle}{\nabla\langle p\rangle} \tag{21}$$

where $\langle u\rangle$ and $\langle p\rangle$ are the superficial velocity and average pressure in the porous GDL respectively.

Fig. 4 shows the permeability of the present 2D porous GDL under different pressure gradients. It is clearly shown that the GDL has higher in-plane permeability than through-plane permeability. This is because more fibers are oriented to the x direction (shown in Fig. 3). The in-plane and through-plane permeability of Tory 090 with porosity 0.80 measured by Gostick et al. [18] are 8.99×10^{-12} m^2 and 2×10^{-11} m^2, respectively. The simulated results in this study are 5.8×10^{-11} m^2 for the in-plane permeability and 2.96×10^{-11} m^2 for the through-plane, which are somewhat greater than the experimental results, partially due to the relatively large porosity (0.87) of the present porous GDL.

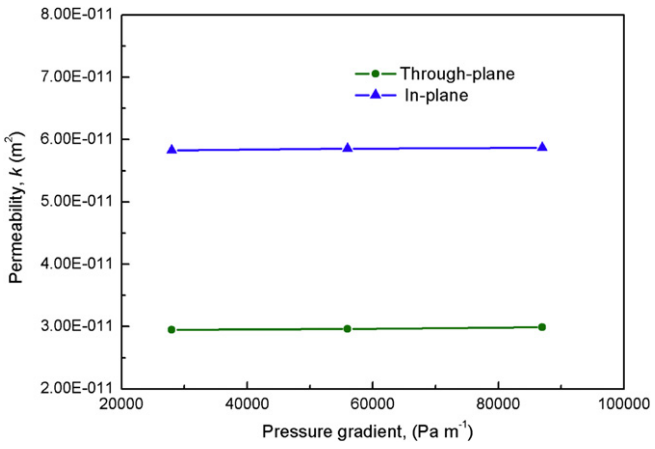

Fig. 4. Numerically predicted permeability of the reconstructed GDL.

4.2. Effective diffusivity of the porous GDL

The effective diffusivity is another important macroscopic effective transport property of the porous GDL [16]. Unfortunately, there have been few researches to measure the anisotropic effective diffusivity of the porous GDL [19]. In this study, gas diffusion simulation is performed to evaluate the effective diffusivity of the present 2D porous GDL using mass transport LB model introduced in Section 2.2. Concentration fractions are specified on the inlet and outlet, keeping the rest two surfaces as no flux boundaries. The solid obstacles in the domain are impermeable objects with no flux boundary conditions on their surfaces. Similar to the simulation in Section 4.1, fifty more lattices are added on the inlet/outlet boundary as buffer zones. The effective diffusivity of the porous GDL can be calculated by

$$D_{\mathrm{eff},x} = \frac{D\left(\int_o^H \frac{\partial X}{\partial x}dy\right)\Big/H}{(X_{\mathrm{in}}-X_{\mathrm{out}})/L},\quad D_{\mathrm{eff},y} = \frac{D\left(\int_o^L \frac{\partial X}{\partial y}\mathrm{d}x\right)\Big/L}{(X_{\mathrm{in}}-X_{\mathrm{out}})/H} \tag{22}$$

for in-plane direction and through-plane direction, respectively. D is the binary diffusivity. H and L are the height and length of the present porous GDL, respectively. X_{in} is the inlet concentration fraction and X_{out} is the outlet concentration fraction.

Nam and Kaviany [16] proposed the following correlation to calculate the effective diffusivity of the GDL

$$D_{\mathrm{eff}} = D\varepsilon\left(\frac{\varepsilon-\varepsilon_p}{1-\varepsilon}\right)^{\alpha} \tag{23}$$

where $\alpha = 0.521$ for the in-plane direction, $\alpha = 0.785$ for the through-plane direction, and $\varepsilon_p = 0.11$. D_{eff}/D calculated by Eq. (23) for porosity 0.87 is 0.758 and 0.707 for the in-plane direction and through-plane direction, respectively. The simulated D_{eff}/D for the in-plane direction and through-plane direction are 0.771 and 0.713, respectively, which are in good agreement with the values calculated by Eq. (23).

4.3. Single-phase simulation

4.3.1. Model development

Whether water generated in PEMFC is in vapor phase or liquid phase depends on the local water saturation pressure. Water vapor will condense to liquid water if the water vapor pressure exceeds the saturation pressure. In the simulation of this section, water is assumed to be in vapor phase only because the inlet humidity of the reactant gases is specified as zero. Under this dry condition, the water vapor pressure is low and the condensation rarely occurs.

Besides the above assumption, the following assumptions are also made during the simulation: the operation condition is considered as isothermal and steady state; all the physical properties of the species are constant; the gas mixtures are assumed to be ideal gas mixtures; the CL is assumed to be ultra-thin and is treated as a reactive interface on the bottom surface of GDL.

To the best of our knowledge, there has been no literature considering the electrochemical reactions when employing LBM to investigate mass transport in PEMFC. In this study, the electrochemical reaction is taken into account in the LB simulation, which is implicitly represented by source term S in Eq. (7). S is zero in the whole computational domain except the CL, since electrochemical

reaction only takes place in CL. In CL, oxygen reduction reaction (ORR) occurs and the source term in physical unit is [8]

$$S_p = \frac{j}{nF} \tag{24}$$

where n is the electron number and equals 4 and 2 for oxygen and water vapor, respectively. F is the Faraday's constant. j is the transfer current density calculated by Tafel equation, which relates the local current density to the local oxygen concentration and over-potential η

$$j = A_v j_{Ref}\left(\frac{C_O}{C_{O,Ref}}\right)^{r_c}\exp\left(-\frac{\alpha F}{RT}\eta\right) \tag{25}$$

where C_O is the oxygen concentration, α is the cathode transfer coefficient, R is the universal gas constant, A_v is the specific reaction surface area per volume of the CL, $C_{O,Ref}$ is the reference oxygen concentration, and γ_c is the ORR reaction order.

Thus, source term S_L in lattice units is calculated by [32]

$$S_L = S_p\frac{t_0}{5C_{total}} \tag{26}$$

where C_{total} is the total concentration of water vapor and oxygen.

Now attention is turned to the boundary conditions. As shown in Fig. 3, velocity and species concentration fraction are given at the inlet and fully-developed boundary condition is adopted at the outlet. Symmetry boundary conditions are used at the left and right boundaries. No slip and no flux boundary conditions are employed on the surface of carbon fibers and land for fluid flow and mass transport, respectively. On the bottom surface, no slip boundary condition is applied for fluid flow; different over-potential values are specified for mass transport, creating different S in Eq. (7) according to Eqs. (24)–(26) and thus resulting in different mass transport flux on the bottom surface. In LBM, the above given velocity condition is achieved by velocity boundary condition [37]; and no slip boundary condition and no flux boundary condition are obtained by using the bounce-back boundary condition [38].

The main steps for performing the simulation are as follows: (1) transforming the physical computational domain into digital text in which the void space is zero and the solid phase is unit; (2) translating variables in physical units to lattice units; (3) simulating the flow field using fluid flow LB model; (4) simulating the oxygen transport and water vapor transport in the flow field using mass transport LB model; (5) transforming variables in lattice units to physical units after simulation convergence is obtained.

In the simulation, if the relative error between successive 200 iterated steps is less than 1×10^{-6}, the simulation convergence is obtained.

4.3.2. Validation

A convective-diffusive-reaction problem is employed to validate the model developed in Section 4.3.1, schematically shown in Fig. 5(a). Concentration fraction at $y = 0$ and H are kept at constant, $X_{in} = 1$ and $X_{out} = 0$. A constant normal flow with velocity v is injected into the domain from $y = 0$ and is removed from $y = H$. Reaction takes place in the whole computational domain. The macroscopic governing equation for concentration fraction of this problem is:

$$v\frac{dX}{dy} = D\frac{d^2X}{dy^2} - kX \tag{27}$$

where k is the reaction rate. Based on the theory of differential equation, the analytical solution of Eq. (27) is

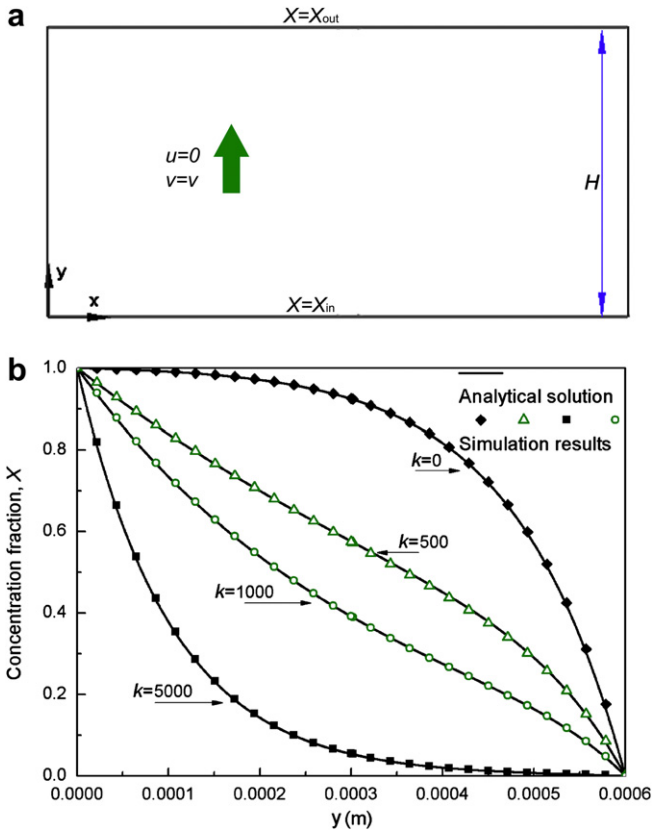

Fig. 5. Convection–diffusion-reaction problem between two parallel plates. (a) Schematic of the problem, (b) comparison between analytical solution and LBM simulation results.

$$X = A_1\exp(B_1 y) + A_2\exp(B_2 y) \tag{28a}$$

where

$$B_1 = \left(\frac{v}{D} - \sqrt{\left(\frac{v}{D}\right)^2 + \frac{4k}{D}}\right)\Big/2, B_2 = \left(\frac{v}{D} + \sqrt{\left(\frac{v}{D}\right)^2 + \frac{4k}{D}}\right)\Big/2,$$

$$A_1 = \frac{X_{out} - X_{in}\exp(B_2 H)}{\exp(B_1) - \exp(B_2 H)}, A_2 = X_{in} - A_1 \tag{28b}$$

In the simulation, $D = 2.845 \times 10^{-5}$ m^2 s^{-1}, $v = 2.845 \times 10^{-2}$ m s^{-1}, $H = 3 \times 10^{-4}$ m. J_0 in Eq. (10) is 0.2. The mesh of the computational domain is 301 × 301. Fig. 5(b) compares the simulation results with the analytical solutions under different reaction rates. It can be seen that the simulation results agree well with the analytical solutions. The maximum deviation is less than 0.02%, indicating that the model developed can predict proper physical behaviors. Thus, we go on further to simulate the fluid flow and mass transport in the computational domain shown in Fig. 3. The simulation results presented below are obtained with the physical parameters and base conditions listed in Table 1.

4.3.3. Velocity vector and mole fraction distribution

Fig. 6 shows the velocity vector distribution of the gas mixtures. It can be seen that gas flows from the inlet channel to the outlet channel through the void space between the carbon fibers, presenting complex flow patterns due to the complicated structures of the GDL. The apparent in-plane flow improves the supply of reactants to reactive site under the land.

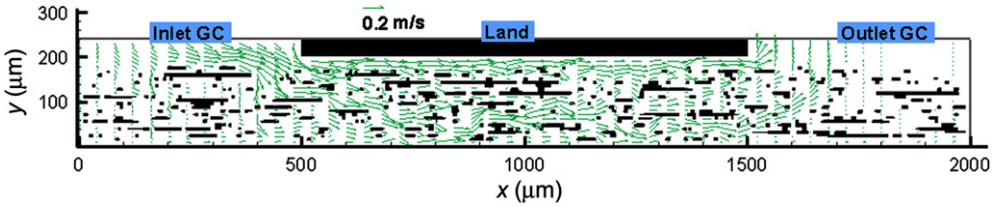

Fig. 6. Velocity distribution in the computational domain.

Fig. 7 shows oxygen mole fraction distributions under different over-potentials specified at the bottom surface. The specified over-potential is 0.3 V, 0.4 V and 0.6 V, respectively. From the inlet GC to the outlet GC, oxygen mole fraction gradually decreases due to the oxygen consumption on the bottom surface. At the outlet, the mole fraction decreases as the specified over-potential increases because more oxygen is consumed under higher over-potential condition. In the right-down corner, the minimal oxygen concentration appears, due to the thickest diffusion layer and smallest velocity in this region [6]. Within the GDL, the oxygen mole fraction profiles are very flexuous and are significantly affected by the porous structures of GDL.

Fig. 8 shows water vapor mole fraction distributions under different over-potentials specified at the bottom surface. The specified over-potential is 0.3 V, 0.4 V and 0.6 V, respectively. From the inlet GC to the outlet GC, the water vapor mole fraction gradually increases due to continual generation of water vapor on the bottom surface. At the outlet, water vapor concentration fraction increases as over-potential increases due to more generation of water vapor under higher over-potential. Similar to the oxygen mole fraction profile, the water vapor mole fraction profiles are also flexuous due to the porous structures of GDL. An interesting phenomenon in Fig. 8 is that maximum water vapor concentration is located in the right-down corner in Fig. 8(a) and (b) (low and moderate over-potentials) while it moves to the center of the bottom surface in Fig. 8(c) (high over-potential). This is because oxygen almost exhausts in the upstream under high over-potential condition, resulting in oxygen starvation in the right-down corner. The oxygen starvation is further exacerbated due to the extremely low local effective diffusivity in the right-down corner (due to the long carbon fiber as shown in Fig. 8(c)). Thus, hardly any water vapor generates in the right-down corner, and water vapor there is mainly diffused from the upstream. This change of the location of maximum vapor concentration is rarely reported in literature based on macroscopic simulations, since uniform diffusivity of GDL is adopted in these simulations which ignore the influence of actual structural morphology of the GDL [5–7]. Clearly, the change of the location of maximum vapor concentration further indicates the important effects of the porous structures.

4.3.4. Local current density distribution

Fig. 9 shows local current density distributions on the bottom surface as a function of x/L, where L is the total length of land and

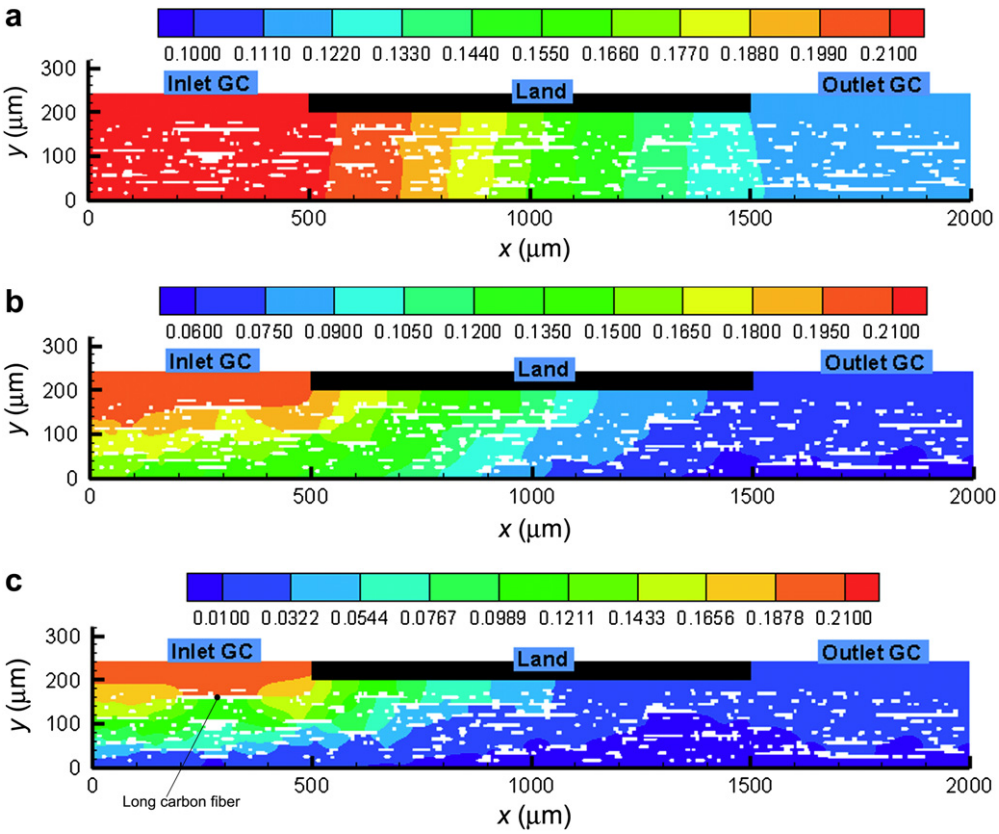

Fig. 7. Oxygen mole fraction distribution under different over-potentials: (a) 0.3 V, (b) 0.4 V, (c) 0.6 V.

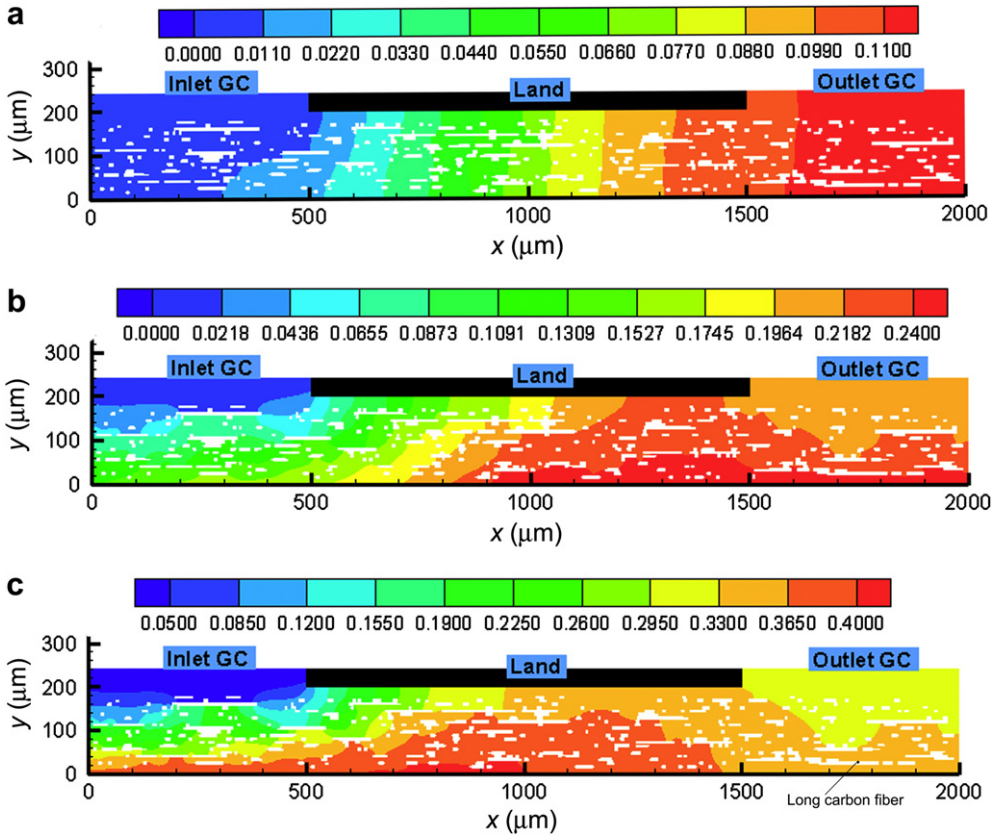

Fig. 8. Water vapor mole fraction distribution under different over-potentials: (a) 0.3 V, (b) 0.4 V, (c) 0.6 V.

channel. In Fig. 9, all the curves suffer a sudden drop around $x = L_1$ because there exists a long cross carbon fiber, as marked in Fig. 7(c). This cross carbon fiber seriously impedes the mass transport in the through-plane direction, resulting in less oxygen available for electrochemical reaction on the bottom surface near $x = L_1$.

The simulation results of Kazim et al. [5] and He et al. [11] are also presented in Fig. 9 for comparison. GDL thickness is 2×10^{-4} m in [5], which is the same with the present study. GDL thickness from 2×10^{-4} m to 1×10^{-3} m is considered in [11], and only the results of GDL thickness 6×10^{-4} m are presented in Fig. 9. As shown in Fig. 9,

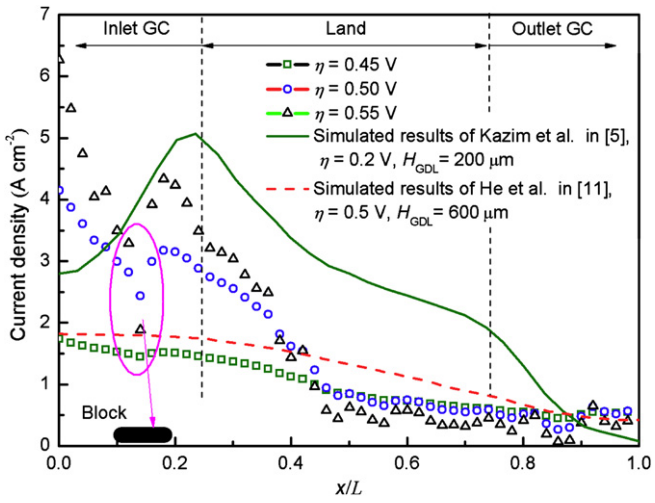

Fig. 9. Local current density distribution under different over-potentials.

the magnitude of the current density predicted by the present simulation is comparable to that in [5] on the whole, but is greater than that in [11]. This is because CL is treated as an ultra-thin interface in the present study and in [5]. This simplified CL may lead to relatively high oxygen concentration available for reaction and thus high local current density is predicted, because oxygen concentration will greatly reduce in the confined void space of a real CL.

In Fig. 9, the distribution characteristic of the current density predicted by the present study differs from that in [5], although GDL thickness in this study is the same with that in Ref. [5]. The maximum current density reported in literature usually appears at $x = L_1$ (inlet GC/land interface) for GDL thickness around 2×10^{-4} m [5,11]. However, it appears at $x = 0$ in this study, which agrees with the results of the case with a thicker GDL (6×10^{-4} m) in [11]. This discrepancy is also caused by the long carbon fiber marked in Fig. 7(c). This long transverse fiber plays the similar effect as a thick GDL does, which creates local thick diffusion layer because most of the air takes the shortest route through the GDL [11].

Clearly, the distinct distribution of the local current density predicted by present LBM simulation again proves the great effects of local porous structures of GDL.

4.4. Two-phase flow simulation

In this section, pore-scale behaviors of liquid water in the GDL of interdigitated PEMFC are investigated using the SC model introduced in Section 2.3. Before implementing the two-phase simulations, it is necessary to calibrate g controlling the fluid–fluid interaction and w controlling fluid–solid interaction in SC model. In this regard, two numerical experiments are conducted: bubble test to evaluate g and static droplet contact angle test to determine w.

4.4.1. Bubble test

The bubble test consists of a circular bubble with radius of 20 lattices initially located at the center of a 100 × 100 lattices system. Based on the work by Huang et al [39], in the bubble initial densities are set as $\rho_1 = 2$ and $\rho_2 = 1 \times 10^{-5}$, and outside the bubble initial densities are set as $\rho_1 = 1 \times 10^{-5}$ and $\rho_2 = 2$, where ρ_1 is the density of gas and ρ_2 is the density of liquid. Periodic boundary conditions are applied on the four boundaries.

Fig. 10 shows the difference between the maximum and minimum density of the gas as a function of g. In the SC model, different phases separate with each other only if the absolute value of g exceeds a critical value $2/(9\rho_0)$, where $\rho_0 = \rho_1 + \rho_2$ [39]. It can be seen that in Fig. 10 that the critical value is about 0.22, which is in good agreement with the theoretical value 0.222. When $g < 0.22$, the density difference is zero indicating different phases mix with each other. When $g > 0.22$, the density difference becomes increasing larger, implying different phases start to separate and the bubble becomes increasingly pure. Overlarge g leads to density difference greater than 2.0 as shown in Fig. 10. Thus, g is set as 0.5 in the following simulation.

The pressure difference across the liquid/gas interface is related to the radius R of the bubble by Laplace's Law

$$p_i - p_o = \sigma/R \tag{29}$$

where p_i and p_o are the pressures inside and outside the bubble, respectively. σ is the surface tension force. Fig. 11 shows the pressure difference Δp as a function of $1/R$, where the inserted image shows a bubble with radius 20 (lattice unit) obtained from the simulations. p_i and p_o are calculated 8 lattices away from the bubble surface, shown by the dashed circles in the inserted image. It can be seen that the pressure difference is proportional to $1/R$, showing a good agreement with Laplace's Law.

4.4.2. Static contact angle test

Contact angle is usually considered as a measure of the solid surface wettability. A surface is wetting or hydrophilic if the contact angle $\theta < 90°$, and liquid tends to spread as film on the solid surface. On the contrary, the surface is non-wetting or hydrophobic if $\theta > 90°$, and liquid tends to form a droplet on the solid surface. A set of initially semicircular static droplets on a horizontal solid surface are simulated to predict different contact angles, with w changing from −0.2 to 0.2. Initial densities are set as $\rho_1 = 1 \times 10^{-5}$ and $\rho_2 = 2$ inside the droplet, and $\rho_1 = 2$ and $\rho_2 = 1 \times 10^{-5}$ outside the droplet. Periodic boundary conditions are applied on the left and right boundaries. No slip boundary conditions are used on the bottom and top boundaries. The droplet radius is calculated by the method proposed in Ref. [40].

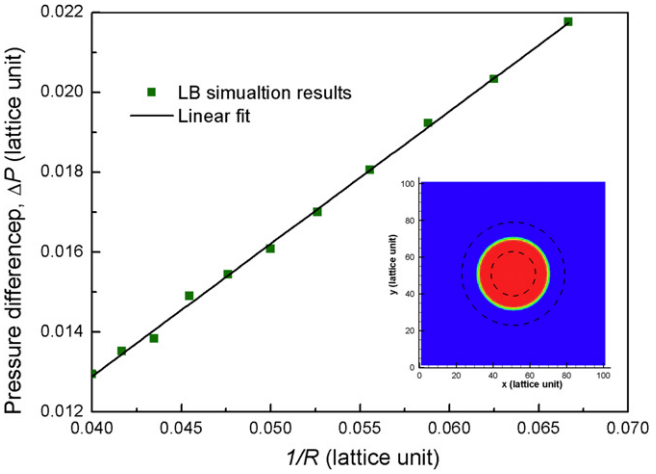

Fig. 11. Pressure difference inside and outside the droplet as a function of the reciprocal of droplet radius $1/R$.

Fig. 12 presents the relationship between w and the predicted contact angles, where the insert image shows droplets with different contact angles. Previous literature reported that the contact angle is a linear function of w [39]. The simulation results show this characteristic in the range of w from −0.1 to 0.2. In the following simulation, different contact angle of the GDL can be obtained by choosing the corresponding w according to Fig. 12.

4.4.3. Liquid water pore-scale behaviors

Now we focus on the simulations of pore-scale behaviors of liquid water. A liquid droplet is initially placed in the middle of the GDL, as shown in Fig. 13(1), which is subjected to the air flow from the inlet GC and moves towards to the outlet GC. In the figure, blue is liquid water, white denotes void space and black represents carbon fiber. Initially, liquid density is 2.0 inside the droplet and 1×10^{-5} outside the droplet, and air density is 1×10^{-5} inside the droplet and 2.0 outside the droplet. Such setting of equal density of

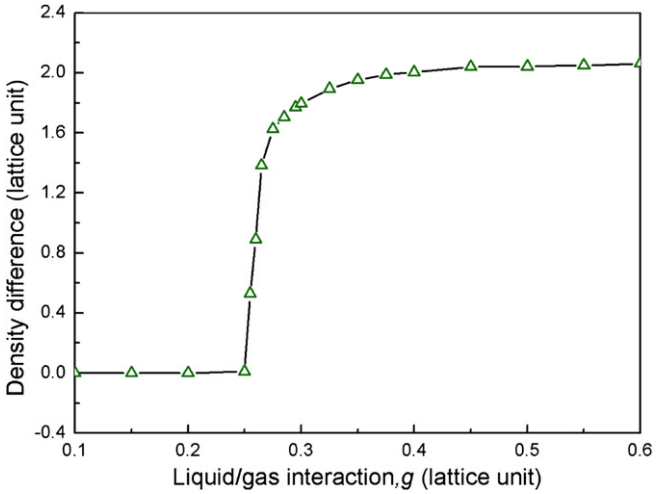

Fig. 10. Difference between the maximum and minimum density of gas as the function of fluid–fluid interaction strength g.

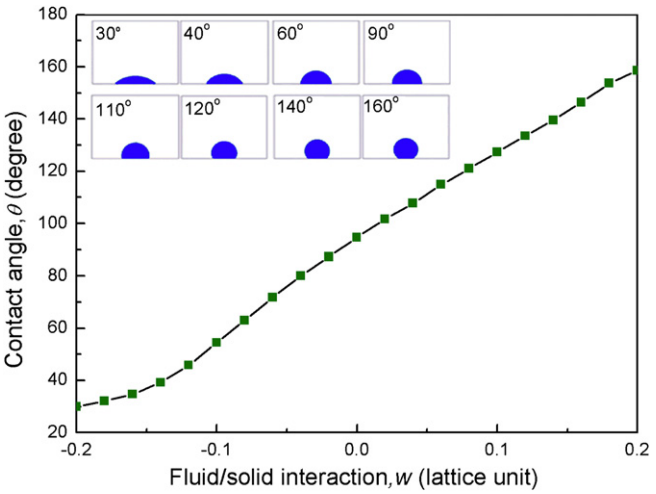

Fig. 12. Contact angles of droplets on the solid surface as a function of fluid–solid interaction w.

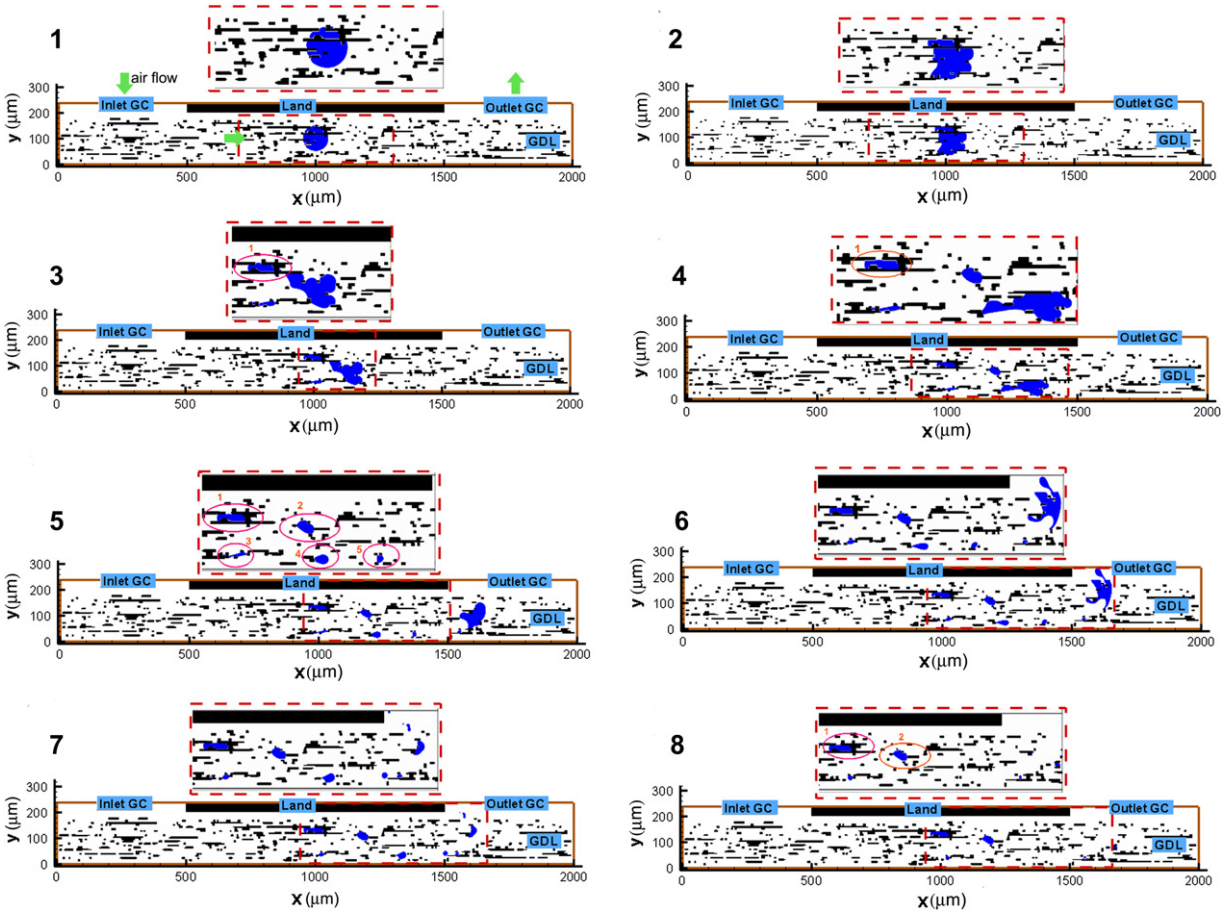

Fig. 13. Pore-scale behaviors of liquid water inside a GDL of interdigitated PEMFC. (black: carbon fibers or land; white: void space; blue: liquid water). 1: $t = 100\ \delta t$ (lattice units), 2: $t = 3000\ \delta t$, 3: $t = 10{,}000\ \delta t$, 4: $t = 28{,}000\ \delta t$, 5: $t = 51{,}000\ \delta t$, 6: $t = 52{,}000\ \delta t$, 7: $t = 54{,}000\ \delta t$, 8: $t = 69{,}000\ \delta t$.

liquid and gas is also employed in Refs. [27,28]. Gas flow velocity is set as 0.05 (lattice unit) at the inlet. Fully developed boundary condition is adopted at the outlet. Symmetry boundary condition is applied on the left and right boundaries. No slip boundary condition is employed on the carbon fiber surfaces, the rib surfaces and the bottom surface. The contact angle of the GDL is 110°.

Fig. 13 displays the time evolution of pore-scale behaviors of the liquid water. At the beginning, liquid water is located under the land as shown in Fig. 13(1). The liquid water starts to migrate due to air flow from the inlet GC, as shown in Fig. 13(2); and it preferentially passes through the largest pores due to the smallest resistance there. In Fig. 13(3) and (4), a fraction of the liquid water (in Circle 1) is trapped in a dead-end pore, and the bulk of the liquid water keeps advancing. The bulk reaches the state shown in Fig. 13(5) after a long time of creeping, with several residues left behind. These residues either are trapped by the dead-ended pores (in Circle 1) or draggled behind the bulk due to their relatively lower velocity (in Circles 2–5). Meanwhile, the bulk keeps moving in a more expediting pathway where air velocity is high, and reaches the outlet GC in less than 1000 time steps, shown in Fig. 13(5–6). In the outlet GC, the bulk is severely torn into several strips and is deflected towards the land under the influence of gas flow as shown in Fig. 13(6). Finally, the bulk is flushed out of the computational domain in Fig. 13(7). Subsequently, residues not trapped are also flushed out of the GDL, shown in Fig. 13(8). Eventually, merely few parts of the GDL are occupied by the liquid water and the flooding problem is significantly alleviated.

Liquid water transport mechanism is capillary fingering in the GDL of PEMFC with parallel flow field where capillary force dominates liquid water transport [22,28]. However, shear force plays an important role on the liquid water behaviors in GDL of interditigated PEMFC, since the gas velocity in the GDL is considerably higher than that in the GDL of parallel PEMFC. The situation of capillary dominated period and shear force dominated period coexists in the present simulation. In Fig. 13(1–5), gas velocity is very small in regions with low local porosity, thus liquid water behaviors show the characteristics of capillary fingering. The liquid water behaviors present following characteristics: first, local pore structures dramatically affect liquid water transport and the liquid water preferentially passes through largest pores; second, liquid water behaviors can be described as slow sleeping. In Fig. 13(6–8), liquid water reaches regions with high air flow, and it is accelerated by the fast gas flow and is rapidly expelled out of the GDL. Under this circumstance it seems that liquid water behaviors are dominated by the shear force.

4.4.4. Effects of land width on liquid removal

There have been several studies regarding the influence of flow field designs on cell performance [10–12]. In this study, emphasis is placed on the effects of land width on the liquid water removal time and liquid water residual saturation. The liquid water saturation in the GDL is defined as the ratio of pore volume occupied by liquid water to the total pore volume. Initial and boundary conditions are the same as that in Section 4.4.3.

Fig. 14 presents the time evolution of liquid water saturation in the GDL with different land widths. In all the simulations, the total width of the land and channel is kept at 2×10^{-3} m; and the inlet GC and outlet GC have the same widths. In Fig. 14, liquid water saturation keeps approximately constant in the initial stage because liquid water still transports inside the GDL. Then the water saturation undergoes a sudden drop, indicating that the bulk of liquid water is already being removed out of the GDL. After the sudden drop, the liquid water saturation maintains constant in the GDL. The final constant liquid water saturation is called residual saturation; and the time required to achieve the residual saturation is called removal time.

In Fig. 14, the removal time decreases as the land width decreases. This is because a narrow land creates faster gas flow within the GDL. A narrow land also means shorter distance between the initial location of liquid water and the GDL outlet. In addition, the residual saturation also reduces as the land width decreases because faster air flow under narrower rib can flush liquid water out of the GDL more efficiently. It is recognized that excessive liquid water in the GDL hinders reactant transport, impedes cold start operation and reduces durability of PEMFC. Therefore, a narrower land is favorable for PEMFC operation and durability. However, the land should not be too narrow because it also serves as pathways for the electron. Commonly, a moderate channel/land width ratio of unit is suggested in literature; and land width of 1×10^{-3} m in the present simulation is just the case. For this case, the residual saturation is only about 0.05, much lower than the initial given water saturation 0.18, indicating that the interdigitated flow fields can effectively alleviate the flooding inside the GDL.

4.4.5. Effects of GDL contact angle

In this section, effects of GDL contact angle on liquid water removal time and residual saturation are investigated. The contact angle varies from 100° to 130° with an increase of 10°. Initial and boundary conditions are the same as that in Section 4.4.3.

Fig. 15 presents the time evolution of liquid water saturation inside the GDL with different contact angles. To better understand the effects of the contact angle, two time parameters t_1 and t_2 are defined. t_1 is the time required for the bulk of liquid water arriving at the GDL outlet (the time of the initially constant saturation period in Fig. 15) and t_2 is the time required for bulk of liquid water passing through the GDL outlet (the time of the sudden drop

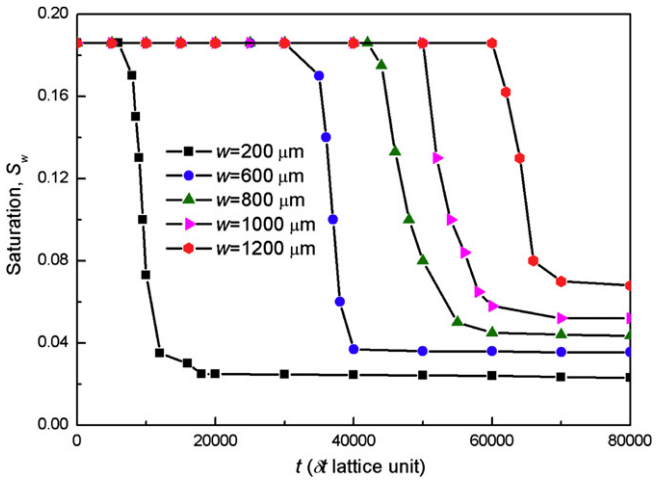

Fig. 14. Time evolution of liquid water saturation inside the GDL with different land widths.

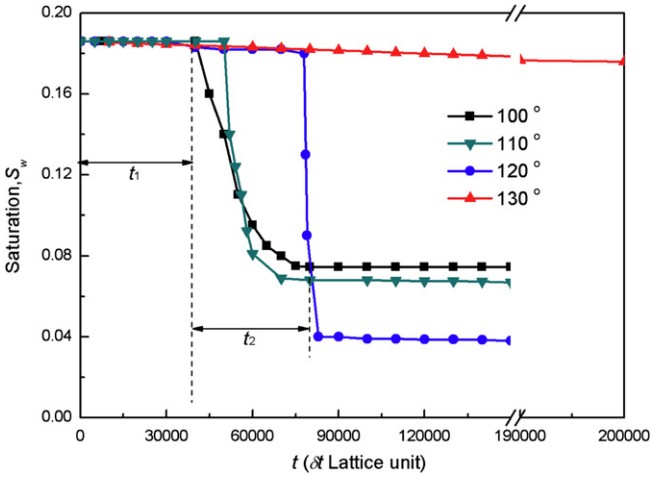

Fig. 15. Time evolution of liquid water saturation inside the GDL with different GDL contact angles.

period). Based on the discussion in Section 4.4.3, it can be concluded that t_1 represents the time of capillary dominated period and t_2 is the time of shear force dominated period.

In Fig. 15, t_1 increases as the contact angle increases, because higher contact angle creates higher resistance against liquid water advancing during capillary force dominated period. On the contrary, t_2 decreases as the contact angle increases, because higher contact angle leads to smaller adhesion between liquid water and the solid surface during the shear force dominated period. This agrees with the simulation results obtained by Li et al. using volume of fluid (VOF) method [20]. Therefore, it can be concluded that a higher contact angle impedes liquid water advancing during capillary force dominated period and facilitates liquid water transport during shear force dominated period.

Obviously, liquid water removal time $(t_1 + t_2)$ is mainly occupied by t_1 because capillary fingering process is extremely slow. Thus, the removal time increases as contact angle increases, as shown in Fig. 15. For contact angle as 130°, the resistance in the capillary dominated period is so high that liquid water has not arrived at the GDL outlet even after 200,000 δt. It also can be seen in Fig. 15 that higher contact angle leads to lower residual saturation because higher contact angle retains less liquid water during the shear force dominated period. However, the residual saturation increases as the contact angle increases in the VOF modeling of Li et al. [20]. This discrepancy may be due to different porous structures of GDL adopted.

5. Conclusion

In this paper, LBM is employed to investigate pore-scale fluid flow and mass transport in the GDL of interdigitated PEMFC. A porous GDL obtained from the structure reconstruction process is adopted in the simulation instead of a homogeneous GDL commonly used in conventional macroscopic continuum models. The results of the present pore-scale simulations show great effects of GDL pore structures on fluid flow, mass transport, local current density distribution and liquid water behaviors. The main conclusions can be derived as follows:

1. The porous structure of GDL is inhomogeneous and the in-plane permeability (effective diffusivity) is higher than the through-plane permeability (effective diffusivity).

2. Pore structures of GDL greatly affect flow field, species concentration distribution and local current density distribution. Compared to homogeneous GDL structures used in conventional macroscopic continuum models, the complex porous structures of GDL in this study lead to the change of location of maximum water vapor concentration, create sudden drop of local current density and result in distinct distribution characteristics of local current density.
3. Pore-scale behaviors of liquid water within the GDL of interdigitated PEMFC can be classified as slow creeping in regions with slow air flow (capillary force dominated) and quick moving in regions with fast air flow (shear force dominated).
4. Narrower land can reduce the liquid water removal time and liquid water residual saturation in the GDL.
5. Higher contact angle impedes liquid water advancing during capillary force dominated period and facilitates liquid water transport during shear force dominated period. On the whole, higher contact angle increases the removal time and reduces the residual saturation.

Acknowledgments

This work is supported by the Key Project of the National Natural Science Foundation of China (50636050, 51136004).

Nomenclature

A_v	specific reaction surface area per volume of the CL (m^{-1})
c_s	speed of sound in LBM
C_O	oxygen concentration (mol m^{-3})
$C_{O,ref}$	reference oxygen concentration (mol m^{-3})
C_Q	lattice dependent coefficient in Eq. (12)
C_{total}	total concentration of oxygen and water vapor (mol m^{-3})
D	diffusivity (m^2 s^{-1})
$\mathbf{e}_i$	discrete velocity in LBM
f_i	particle distribution function in the ith direction
f_i^{eq}	equilibrium particle distribution function
F	Faraday's constant (C mol^{-1})
$\mathbf{F}_{a,k}$	fluid–solid interaction force in SC model
$\mathbf{F}_{c,k}$	fluid–fluid surface tension acting on kth component in SC model
$\mathbf{F}_k$	forces acting on kth component
g	parameter control strength between different component in SC model
$G_{k\bar{k}}$	Green function in SC model
H	height (m)
j_{ref}	reference exchange current density (A m^{-3})
j	transfer current density (A m^{-3})
J_i	specially chosen constant in Eq. (8)
K_i	specially chosen constant in Eq. (8)
l_0	length scale
n	electron number
p	Pressure (Pa)
$\langle p \rangle$	average pressure (Pa)
R	universal gas constant (J mol^{-1} K^{-1})
s	an indicator function in Shan and Chen model for solid phase
S	source term in mass transport LB model
t	time
t_0	time scale
Δt	time step
T	temperature of the operation condition (K)
$\mathbf{u}$	local velocity (m s^{-1})
$\mathbf{u}'$	common velocity for all of the phases in SC model (m s^{-1})
$\langle u \rangle$	superficial velocity (m s^{-1})
w	parameter controls strength between fluid and wall in SC model
w_i	weight factor in equilibrium particle distribution function
W	Green function SC model
x	position
Δx	mesh width
X_k	mole fraction of kth species

Greek symbol

α	cathode transfer coefficient in Eq. (22)
β	residual error
ε	porosity
ε_p	parameter in Eq. (23)
γ_c	ORR reaction order
η	over potential
σ	surface tension
υ	Kinetic viscosity
ρ	Density
τ	relaxation time
τ_υ	relaxation time related to viscosity
τ_D	relaxation time related to diffusivity
ψ_k	effective density in SC model

Subscripts and superscripts

in	inlet
L	lattice unit
p	physical unit
out	outlet

References

[1] T.E. Springer, T.A. Zawodzinski, S. Gottesfeld, Polymer electrolyte fuel cell model, Journal of The Electrochemical Society 138 (1991) 2334–2342.
[2] H. Li, Y. Tang, Z. Wang, Z. Shi, S. Wu, D. Song, J. Zhang, K. Fatih, J. Zhang, H. Wang, Z. Liu, R. Abouatallah, A. Mazza, A review of water flooding issues in the proton exchange membrane fuel cell, Journal of Power Sources 178 (2008) 103–117.
[3] T.V. Nguyen, A gas distributor design for proton-exchange-membrane fuel cells, Journal of the Electrochemical Society 143 (1996) L103–L105.
[4] D.L. Wood, J.S. Yi, T.V. Nguyen, Effect of direct liquid water injection and interdigitated flow field on the performance of proton exchange membrane fuel cells, Electrochimica Acta 43 (1998) 3795–3809.
[5] A. Kazim, H.T. Liu, P. Forges, Modelling of performance of PEM fuel cells with conventional and interdigitated flow fields, Journal of Applied Electrochemistry 29 (1999) 1409–1416.
[6] M. Hu, X. Zhu, M. Wang, A. Gu, L. Yu, Three dimensional, two phase flow mathematical model for PEM fuel cell: part II. Analysis and discussion of the internal transport mechanisms, Energy Conversion and Management 45 (2004) 1883–1916.
[7] M. Hu, A. Gu, M. Wang, X. Zhu, L. Yu, Three dimensional, two phase flow mathematical model for PEM fuel cell: part I. Model development, Energy Conversion and Management 45 (2004) 1861–1882.
[8] G. Hu, J. Fan, S. Chen, Y. Liu, K. Cen, Three-dimensional numerical analysis of proton exchange membrane fuel cells (PEMFCs) with conventional and interdigitated flow fields, Journal of Power Sources 136 (2004) 1–9.
[9] L. Wang, H. Liu, Performance studies of PEM fuel cells with interdigitated flow fields, Journal of Power Sources 134 (2004) 185–196.
[10] J.S. Yi, T. Van Nguyen, Multicomponent transport in porous electrodes of proton exchange membrane fuel cells using the interdigitated gas distributors, Journal of The Electrochemical Society 146 (1999) 38–45.
[11] W. He, J.S. Yi, T.V. Nguyen, Two-phase flow model of the cathode of PEM fuel cells using interdigitated flow fields, Materials, Interfaces, and Electrochemical Phenomena 46 (2000) 2053–2064.
[12] M. Grujicic, C.L. Zhao, K.M. Chittajallu, J.M. Ochterbeck, Cathode and interdigitated air distributor geometry optimization in polymer electrolyte membrane (PEM) fuel cells, Materials Science and Engineering B 108 (2004) 241–252.
[13] W. He, G. Lin, T.V. Nguyen, Diagnostic tool to detect electrode flooding in proton-exchange-membrane fuel cells, AIChE Journal 49 (2003) 3221–3228.
[14] K. Ito, K. Ashikaga, H. Masuda, T. Oshima, Y. Kakimoto, K. Sasaki, Estimation of flooding in PEMFC gas diffusion layer by differential pressure measurement, Journal of Power Sources 175 (2008) 732–738.
[15] J.T. Gostick, M.W. Fowler, M.A. Ioannidis, M.D. Pritzker, Y.M. Volfkovich, A. Sakars, Capillary pressure and hydrophilic porosity in gas diffusion layers

for polymer electrolyte fuel cells, Journal of Power Sources 156 (2006) 375–387.
[16] J.H. Nam, M. Kaviany, Effective diffusivity and water-saturation distribution in single- and two-layer PEMFC diffusion medium, International Journal of Heat and Mass Transfer 46 (2003) 4595–4611.
[17] J.P. Feser, A.K. Prasad, S.G. Advani, Experimental characterization of in-plane permeability of gas diffusion layers, Journal of Power Sources 162 (2006) 1226–1231.
[18] J.T. Gostick, M.W. Fowler, M.D. Pritzker, M.A. Ioannidis, L.M. Behra, In-plane and through-plane gas permeability of carbon fiber electrode backing layers, Journal of Power Sources 162 (2006) 228–238.
[19] J.G. Pharoah, K. Karan, W. Sun, On effective transport coefficients in PEM fuel cell electrodes: anisotropy of the porous transport layers, Journal of Power Sources 161 (2006) 214–224.
[20] J.W. Park, K. Jiao, X. Li, Numerical investigations on liquid water removal from the porous gas diffusion layer by reactant flow, Applied Energy 87 (2010) 2180–2186.
[21] K.J. Lee, J.H. Nam, C.J. Kim, Pore-network analysis of two-phase water transport in gas diffusion layers of polymer electrolyte membrane fuel cells, Electrochimica Acta 54 (2009) 1166–1176.
[22] P.K. Sinha, P.P. Mukherjee, C.Y. Wang, Impact of GDL structure and wettability on water management in polymer electrolyte fuel cells, Journal of Materials Chemistry 17 (2007) 3089–3103.
[23] T. Koido, T. Furusawa, K. Moriyama, An approach to modeling two-phase transport in the gas diffusion layer of a proton exchange membrane fuel cell, Journal of Power Sources 175 (2008) 127–136.
[24] S.Y. Chen, G.D. Doolen, Lattice Boltzmann method for fluid flows, Annual Review of Fluid Mechanics 30 (1998) 329–364.
[25] X.D. Niu, T. Munekata, S.A. Hyodo, K. Suga, An investigation of water-gas transport processes in the gas-diffusion-layer of a PEM fuel cell by a multiphase multiple-relaxation-time lattice Boltzmann model, Journal of Power Sources 172 (2007) 542–552.
[26] J. Park, M. Matsubara, X. Li, Application of lattice Boltzmann method to a micro-scale flow simulation in the porous electrode of a PEM fuel cell, Journal of Power Sources 173 (2007) 404–414.
[27] J. Park, X. Li, Multi-phase micro-scale flow simulation in the electrodes of a PEM fuel cell by lattice Boltzmann method, Journal of Power Sources 178 (2008) 248–257.
[28] P.P. Mukherjee, C.Y. Wang, Q. Kang, Mesoscopic modeling of two-phase behavior and flooding phenomena in polymer electrolyte fuel cells, Electrochimica Acta 54 (2009) 6861–6875.
[29] L. Hao, P. Cheng, Lattice Boltzmann simulations of water transport in gas diffusion layer of a polymer electrolyte membrane fuel cell, Journal of Power Sources 195 (2010) 3870–3881.
[30] L. Hao, P. Cheng, Lattice Boltzmann simulations of anisotropic permeabilities in carbon paper gas diffusion layers, Journal of Power Sources 186 (2009) 104–114.
[31] P.L. Bhatnagar, E.P. Gross, M. Krook, A model for collision processes in gases. I. small amplitude processes in charged and neutral one-component systems, Physical Review 94 (1954) 511.
[32] S.P. Dawson, S. Chen, G.D. Doolen, Lattice Boltzmann computations for reaction-diffusion equations, Journal of Chemical Physics 98 (1993) 1514–1523.
[33] S.P. Sullivan, F.M. Sani, M.L. Johns, L.F. Gladden, Simulation of packed bed reactors using lattice Boltzmann methods, Chemical Engineering Science 60 (2005) 3405–3418.
[34] X. Shan, H. Chen, Lattice Boltzmann model for simulating flows with multiple phases and components, Physical Review E 47 (1993) 1815–1819.
[35] X. Shan, G. Doolen, Multicomponent lattice-Boltzmann model with interparticle interaction, Journal of Statistical Physics 81 (1995) 379–393.
[36] N.S. Martys, H. Chen, Simulation of multicomponent fluids in complex three-dimensional geometries by the lattice Boltzmann method, Physical Review E 53 (1996) 743–750.
[37] Q.S. Zou, X.Y. He, On pressure and velocity boundary condition for lattice Boltzmann BGK model, Physics of Fluids 9 (1997) 1591–1598.
[38] D.P. Ziegler, Boundary conditions for lattice Boltzmann simulations, Journal of Statistical Physics 71 (1993) 1171–1177.
[39] H. Huang, D.T. Thorne, M.G. Schaap, M.C. Sukop, Proposed approximation for contact angles in Shan-and-Chen-type multicomponent multiphase lattice Boltzmann models, Physical Review E 76 (2007) 066701.
[40] F. Dullien, Porous Media: Fluid Transport and Pore Structure. Academic Press, San Diego, 1992.
[41] Q. Wang, M. Eikerling, D. Song, Z. Liu, T. Navessin, Z. Xie, S. Holdcroft, Functionally graded cathode catalyst layers for polymer electrolyte fuel cells I. theoretical modeling, Journal of The Electrochemical Society 151 (2004) A950–A957.